# PYROLYSIS RATE AND YIELD STRENGTH REDUCTION IN CARBON FIBER AND GLASS FIBER COMPOSITES UNDER REENTRY HEATING CONDITIONS

**Benton R. Greene[(1)] and Chris L. Ostrom[(2)]**

*[(1)] Jacobs JETS Contract, NASA Johnson Space Center, 2101 NASA Pkwy XI5-9E, Houston, TX 77058, USA, benton.r.greene@nasa.gov*
*[(2)] HX5 Jacobs JETS Contract, NASA Johnson Space Center, 2101 NASA Pkwy XI5-9E, Houston, TX 77058, USA, christopher.l.ostrom@nasa.gov*



## ABSTRACT

The behavior of composite materials, specifically carbon fiber-reinforced polymer (CFRP) and glass fiber-reinforced polymer (GFRP), under re-entry conditions poses a problem for orbital debris re-entry risk modeling. Since these materials pyrolyze rather than melt and their different components demise at different rates, modeling their destruction to determine ground impact risk is complex. Modern spacecraft are using these materials in ever-greater quantities owing to their superior strength-to-weight characteristics, and this has required that the orbital debris community improve its understanding of how these materials demise on re-entry.

In 2019, the NASA Orbital Debris Program Office (ODPO) undertook an extensive test campaign to better understand the rate at which several types of GFRP and CFRP materials pyrolyze under re-entry heating conditions and how that pyrolysis affects their ultimate strength. GFRP with a polyester resin (G10/FR-4) and CFRP with epoxy, cyanate ester, vinyl ester, and phenolic resins were tested. The test campaign was carried out at the Inductively Coupled Plasma (ICP) Torch Facility at the University of Texas at Austin. Because the ICP facility operates in a shirt-sleeve environment, test samples can be changed within seconds or minutes, allowing many samples to be tested in a short period. Two nominal heat flux rates, 20 $W/cm^2$ and 30 $W/cm^2$, and two oxygen concentration conditions, 0% and 2% of atmospheric (*i.e.*, 0% and 0.4% absolute oxygen concentration), were applied to all five types of material. To measure both the char rate and the effect of pyrolysis on the ultimate strength of the material, two types of tests were carried out for each material: a char rate test on a ~10 mm-thick sample of material and an in-situ bending stress test of a ~2 mm-thick sample of material.

Measurements of the char rate showed very similar average pyrolysis front velocity in epoxy resin CFRP as in G10 at 3.6 mm/min and 3.4 mm/min, respectively. However, the total mass loss rate in the G10 was nearly double that of the CFRP at 3.8 g/min and 2.2 g/min, respectively. This result represented a slow ablation rate of carbon fibers in the CFRP at the temperatures encountered in low Earth orbit re-entry and a comparatively rapid removal of the glass fibers in G10 due to melting and spallation. Pyrolysis front velocity was more significantly affected by the type of polymer than the type of fiber, with the cyanate ester CFRP samples displaying an average pyrolysis front velocity of only 1.9 mm/min.

Similarly, the effect of thermal exposure on the ultimate strength of the material depended heavily on the type of polymer and very little on the type of fiber in the material. Epoxy, vinyl ester, and polyester resins all behaved very similarly, with complete structural failure at between 400 J/g and 600 J/g of specific absorbed heat. Phenolic and cyanate ester resins, on the other hand, displayed a change in structural properties that was only barely measurable with the current apparatus even after the maximum exposure time tested.

These data are being incorporated into a numerical model of the ablation and demise of composite materials that will be used to more accurately calculate the ground casualty risk of future spacecraft.

## 1 Introduction

Atmospheric re-entry of orbital debris has been a problem since the very first orbiting spacecraft was launched and has been studied throughout the history of space flight. Today, proposed spacecraft must demonstrate through re-entry simulations that any debris that might survive atmospheric re-entry has less than a 1:10,000 probability of causing any human casualty. One of the NASA Orbital Debris Program Office (ODPO) tasks is to maintain tools to assess this

re-entry risk and advise space operators on safety best practices.

Changing trends in the materials used for spacecraft design have necessitated updating the assumptions used in modeling spacecraft re-entry and breakup to account for the differences in the response of new materials to extreme temperatures.

### 1.1 Current Modeling Approach

For spacecraft that use traditional materials such as aluminum, steel, titanium, and even gallium arsenide in solar panels, aerothermal demise can be modeled as a straightforward calculation of aerodynamic heat absorbed vs. that needed to cause the material to melt or vaporize. However, for newer materials like glass fiber- and carbon fiber-reinforced polymers (GFRP and CFRP, respectively), the calculation is not so simple.

Fiber-reinforced polymer (FRP) composites respond very differently to the elevated temperatures of re-entry. Rather than melting, the polymer matrix pyrolyzes and forms a char layer that can insulate deeper material from the elevated temperature and may continue to hold the fiber strands together. Even if most of the matrix is burned away, the pure carbon fibers can maintain their strength up to 3,000 K. Depending on how the fibers are interwoven, this may prevent aerodynamic forces from shredding the remaining fibers into harmless wisps of material.

Until recently, all of these potential problems were assumed to be negligible, and fiber-reinforced polymers were considered to demise when the material reached the glass transition temperature or the char temperature of the matrix material. Once the matrix material reached this point, it was assumed that the reinforcing fibers would be more or less immediately shredded by aerodynamic forces. The discovery of composite overwrapped pressure vessel (COPV) style tanks surviving intact to the ground [1], as well as a study of the demisability of COPVs performed by Hyperschall Technologie Göttingen (HTG) [2], began to sow doubt about the validity of this assumption.

### 1.2 Modeling FRPs

It is clear that the current approach is insufficient to produce results of the required fidelity and a new approach is needed that accounts for the charring properties of the matrix and the weave and composition of the fibers. The fidelity of this model must balance the risk assessment accuracy against the need for rapid calculations.

An appropriate model for re-entering FRP components approximates the pyrolysis process for a given matrix material and determines rate of char formation in a component, the amount of residual material in the charred matrix, and the degree to which that residual material still holds the fibers together. It also needs to model the ablation, melting, or vaporization of the fiber material. If the fiber material does not demise, the model needs to account for the aerodynamic shear force necessary to remove the exposed fibers from the material surface.

Despite the increasing amount of FRP materials being used on spacecraft, very little published work is available for how such materials behave in the re-entry environment. One-dimensional heat transfer through a charring graphite epoxy composite was investigated as far back as 1980 using a continuous wave $CO_2$ laser energy source to produce surface heat fluxes of up to 2.79 kW/cm$^2$ [3]. There is, however, a large body of work on the behavior of composites in a fire environment, which is analogous though with a much lower typical heat flux. Some of this work is summarized by Blasi [4] and in Chapter 8 of *Composite Materials* [5].

A very simple model for mass loss rate from charring graphite epoxy, for example, was presented by Hidalgo, *et al.*, which uses results from thermogravimetric analysis (TGA) of the given material [6]. However, this model was only validated with samples being exposed to a heat flux rate of 3 W/cm$^2$, an order of magnitude lower than that typical of low Earth orbit (LEO) atmospheric re-entry. McKinnon, *et al.*, measured the changes in thermal transport properties as a composite undergoes pyrolysis using a combination of modeling and a series of experimental procedures [7]. Other researchers have studied graphite epoxy degradation under heat fluxes up to 7.5 W/cm$^2$ [8] [9] [10] and one up to 18 W/cm$^2$ [11].

Understanding the residual strength of charred composite materials both during and after heating is also essential to a good model of component demise on re-entry. This will help determine the breakup of larger assemblies into smaller components as well as the aerodynamic shear force necessary to shred exposed fibers. Once again, some direction in this area can be found in the fire sciences, where many researchers have experimentally investigated the change in structural properties of graphite epoxy composites under extreme heat conditions [12] [13] [14] [15].

### 1.3 Results of Phase I

The NASA ODPO conducted a Phase I Re-entry Survivability Test Campaign study in March 2018 to acquire preliminary data on how CFRP and GFRP materials respond to re-entry conditions [1]. In these tests, many of the CFRP samples took longer to demise than the typical duration of aerodynamic heating during re-entry. Reference [1] contains a full description of the tests and analysis of the results.

In those tests, cylindrical samples of GFRP, CFRP, and Kevlar® fiber-reinforced polymer (manufactured by E.I. du Pont de Nemours and Co.), were exposed to atmospheric re-entry temperatures and the time required for complete destruction of the material was measured.

While the Kevlar fiber demised very quickly, the GFRP and CFRP took several minutes to demise, and in the absence of any oxidative process, the CFRP completely failed to demise, maintaining some structure even after 5 minutes of exposure. These results prompted an update to the NASA re-entry prediction models: the Object Reentry Survival Analysis Tool (ORSAT) and the Debris Assessment Software (DAS) utility. ORSAT now treats CFRP components as a mixture of an epoxy matrix that demises readily and a carbon substrate that survives nearly intact, and DAS assumes that all CFRP materials will survive [1].

The current ORSAT and DAS models, while believed by the ODPO to be appropriately conservative given the current state of understanding, are not a complete depiction of the re-entry demisability of FRP materials. More information is needed to understand how a high-temperature, high-shear stress environment degrades and eventually destroys these materials.

## 2 Experimental Methods

To develop a sufficiently accurate model of FRP re-entry demise, several gaps in understanding need to be filled: the rate at which the material chars, the residual mass of charred matrix material, the residual strength of the charred matrix, and the degree to which the fibers interlocking in a weave pattern resist shredding by aerodynamic shear. Phase II of the ODPO's Re-entry Survivability Test Campaign is designed to address the first three of these knowledge gaps.

As discussed in the Phase I paper, CFRP appears to be the least demisable of the FRP materials tested, so Phase II focuses on this material, though G10 fiberglass is also studied, as it is a very common material in printed circuit boards. The results need to be broadly generalizable, so several varieties of resin matrix are studied at different oxygen and heat fluxes.

The tests conducted in Phase II are designed to answer the following questions for as many resin matrices and at as many relevant conditions as possible:

- At what rate does the resin pyrolysis front travel through the virgin material, and how is this rate affected by the heat flux, resin type, and thickness of unremoved char material?
- How much residual char remains after the resin has completely pyrolyzed?
- How is the structural strength of the material degraded with temperature, char progression, and ablation?
- Once a partially charred FRP cools, what is the residual structural strength of the remaining mixture of virgin and charred material?

Three tests were devised to answer these questions:

- *Char Rate* – Expose a sample coupon to a plasma flow for varying amounts of time and measure the total mass lost and the depth of charred material at the end of each time span. During exposure, measure the stagnation point temperature and backside temperature of the sample.
- *In-Situ Strength* – Expose a sample to a plasma flow while applying a constant 4-point bending load and measure the stagnation point temperature, backside temperature, and strain of the sample throughout exposure.
- *Residual Strength* – Expose a sample to plasma flow under unloaded conditions for varying lengths of time. Measure stagnation point and backside temperature during exposure. After returning to room temperature, load the sample in a 4-point bend and measure load, strain, and ultimate strength of the partially charred sample.

### 2.1 Plasma Torch Facility

The Inductively Coupled Plasma (ICP) facility is in the University of Texas at Austin Wind Tunnel Labs and consists of a 50 kW inductively coupled plasma generator, pictured in Fig. 1. The facility operates at room pressure and provides easy access for changing test samples and instrument probes. Room pressure operation also allows for excellent optical access for many remote measurements like optical pyrometers and video cameras. The torch itself can generate plasma streams of argon or air plasma at flow rates up to 80 slpm and temperatures up to 7,000 K for air and 10,000 K for argon [16]. The diameter of the plasma plume is 30 mm.

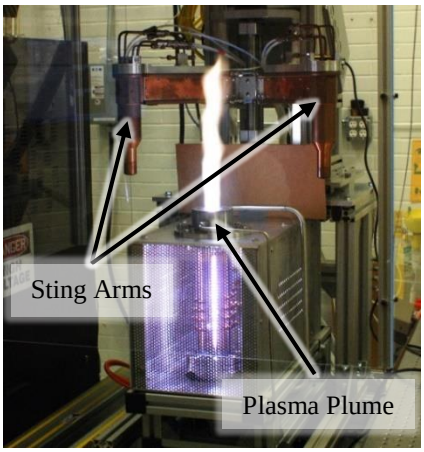


*Figure 1. ICP in operation*

The facility provides two water-cooled, motorized sting arms, also shown in Fig. 1, for mounting test samples and instrument probes. The water-cooling allows the probe or sample to be inserted into the plasma stream for an indefinite period.

## 2.2 Test Samples

Over 230 individual samples were tested in this campaign to maximize the number of tests, conditions, and repeated data points. Because so many samples needed testing, the shape of the test samples was chosen to minimize the time to change out samples between tests and to minimize complexity of the test sample holder.

All test samples were cut to be the same planform size rectangular coupon. The rectangular coupon shape allowed a 4-point bending load to be easily applied to the sample during exposure to the plasma using a simple set of counterweighted jaws. This same set of counterweighted jaws could be used to hold all of the other samples not being placed under load by simply changing the offset of the lower jaws from the upper one.

Two basic sample shapes were used: a 7- to 10-mm-thick rectangular coupon for the char/ablation rate tests and a 1- to 3-mm-thick rectangular coupon, for the static loading tests. All of the coupons were 80 ± 0.7 mm long by 25 ± 0.2 mm wide. The exact thickness of the coupon depended on the available stock of the given material.

Of the several materials used in the test campaign, two materials were exposed to every test condition: the DragonPlate® Economy Plate carbon fiber epoxy panel and the G10 fiberglass panel. DragonPlate is the tradename for the engineered carbon fiber composites made by ALLRed & Associates Inc. under the DragonPlate® brand. These two materials were chosen as broadly representative of the two most common types of composite material aboard spacecraft. Many structural panels are made of a carbon fiber epoxy composite, and most circuit boards are made with a G10 or FR-4 fiberglass composite material. Other materials used were:

- DragonPlate High Temp carbon fiber panel
- CFRP face sheet/Al honeycomb core panel
- Hand layup carbon fiber/vinyl ester resin composite panel
- Hand layup carbon fiber/epoxy resin composite panel
- Carbon fiber/cyanate ester resin composite panel
- Carbon fiber/phenolic resin composite panel

Except for the DragonPlate High Temp panel, these other composites were manufactured in-house at the NASA Johnson Space Center (JSC) machine shop. The cyanate ester resin panel, phenolic resin panel, and the CFRP/aluminum honeycomb panel were taken from off-cuts of other projects to incorporate actual production materials into the test campaign. Tab. 1 gives the number of samples of each material used for each test.

*Table 1. Quantity of coupons of each material used in each test*

| Material | Test | Quantity |
|---|---|---|
| **DragonPlate Economy Plate** | Char Rate | 34 |
| | In-Situ Strength | 8 |
| | Residual Strength | 24 |
| **G10 Fiberglass** | Char Rate | 32 |
| | In-Situ Strength | 8 |
| | Residual Strength | 24 |
| **DragonPlate High Temp** | In-Situ Strength | 8 |
| **CFRP/Al honeycomb** | Char Rate | 2 |
| **CFRP – Vinyl Ester Resin (Hand Layup)** | In-Situ Strength | 8 |
| | Residual Strength | 24 |
| **CFRP – Epoxy Resin (Hand Layup** | In-Situ Strength | 8 |
| | Residual Strength | 24 |
| **CFRP – Cyanate Ester Resin** | Char Rate | 10 |
| | In-Situ Strength | 8 |
| | Residual Strength | 8 |
| **CFRP – Phenolic Resin** | Char Rate | 8 |

## 2.3 Test Setup

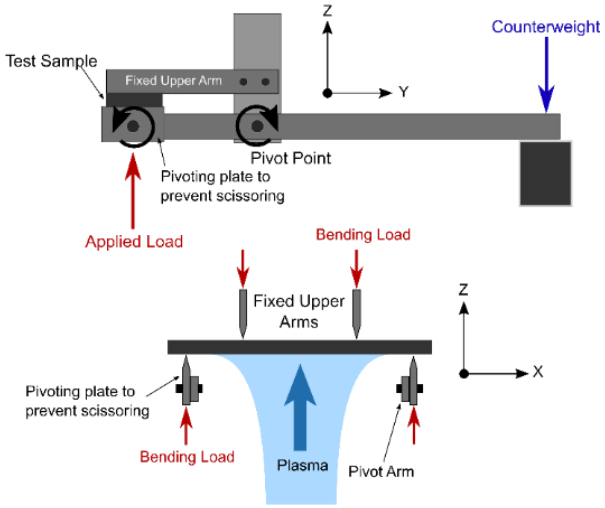


*Figure 2. Diagram of counterweight bending load application*

The sample coupons were mounted in the counter-weighted clamp system pictured in Fig. 2. This system allowed a quick (~10 sec.) installation and removal of

the sample and provided a mechanism for applying a repeatable 4-point bending load to a sample during the In-Situ Strength tests.

Due to the varying test coupon thicknesses among the material specimens, multiple counterweight values were needed to make the bending stress more comparable across tests. Tab. 2 lists the counterweight mass and resulting bending load used for each tested material. Because the load is applied from the bottom of the sample, the actual applied load depends on the weight of the sample. The applied load is calculated using Eq. 1, where $W_C$ is the counterweight value, $W_P$ is the weight of the pivot arm, $W_S$ is the weight of the sample, $D_C$ is the distance from the counterweight to the pivot point, $D_F$ is the distance from the applied load to the pivot point, and $D_P$ is the distance from the center of mass of the pivot arm to the pivot point.

$$F = W_C\left(\frac{D_C}{D_F}\right) + W_P\left(\frac{D_P}{D_F}\right) - W_S \quad (1)$$

The weights of the samples range from 2 g to 10 g. Even for the lowest mass counterweight, this accounts for less than a 5% variance in the applied load to the sample. The masses of the counterweights and the mass of the pivot arm were measured using an AND FX-600 Electronic Balance with a NIST-traceable calibration.

*Table 2. Counterweight and bending load used for each test material*

| CW Mass | Load | Samples |
|---|---|---|
| 110 g | 2 N | Epoxy Resin<br>Vinyl Ester Resin |
| 326 g | 6 N | Epoxy Resin<br>Vinyl Ester Resin |
| 493 g | 9 N | DragonPlate<br>DragonPlate High-Temp<br>G10<br>Cyanate Ester |
| 819 g | 15 N | DragonPlate High-Temp<br>Cyanate Ester |

For tests in which a bending load was not applied, the fixed upper arms in the clamping mechanism were repositioned to be directly above the lower pivot arms.

## 3 Measurements

Several key quantities were measured for all of the tests performed. These were:

- Stagnation surface temperature – measured using an infrared pyrometer
- Back surface temperature – measured using a FLIR thermal imaging camera
- Cold-wall heat flux – measured before and after each test using a Gardon gauge
- Sample mass – measured before and after each test

For the Char Rate and Residual Strength tests, these are the only quantities measured during the experiment itself. During the In-Situ Strength test, the deflection under load of the test sample coupon was also captured using a visible spectrum video camera. Digital image processing was later used to extract the actual sample deflection over time from the video.

### 3.1 Thermal Imaging and Pyrometry

During each test, the stagnation point and back side temperatures of the test coupon were measured using an infrared pyrometer and a FLIR thermal imaging camera, respectively.

The infrared pyrometer was aligned such that it measured the surface temperature at the center point of the impinging plasma jet throughout the test. The pyrometer had a temperature range of 800 K to 3000 K.

### 3.2 Deflection Under Load

To measure the deflection of the test coupon under load during the in-situ strength test, a video camera was placed such that it had an unobstructed view of the edge of the coupon. Before testing began, a calibration image was captured to locate the load points and find the pixel to millimeter conversion ratio.

The videos of each test were post-processed to extract the sample edge location as a function of time throughout the test.

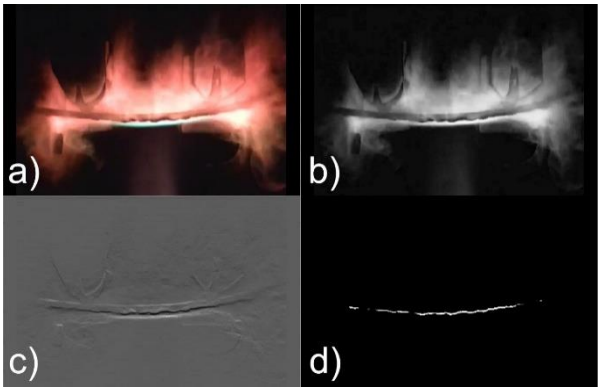


*Figure 3. Sample filter progression. a) Original image. b) Contrast-stretched grayscale image. c) Contrast-stretched gradient image. d) Binarized image showing detected test sample edge*

Fig. 3 shows the progression of the filtering process. Once the image is desaturated (Fig. 3b), either a difference of Gaussians or a directional gradient filter is applied to find the edges in the image. The filtered image then is contrast-stretched (Fig. 3c). Finally, a threshold filter is applied to find the edge of the sample (Fig. 3d). If necessary, the final binary image can be

refined by ignoring white areas that are too small or are outside of some range of expected locations.

The locations of the white pixels in each video frame are then converted to millimeters of sample deflection using the conversion ratio calculated from the calibration image.

### 3.3 Char Density and Extent

While the rectangular shape of the coupons greatly simplified the sample installation and extraction, it created some problems for inferring the char depth from the mass loss. To circumvent these problems, the actual char depth of each sample was measured using x-ray computed tomography. In the resulting scan volumes, the transmissivity of the charred material was measurably higher than that of the virgin material, so a threshold filter could be applied to find the volume of the whole sample and the volume of the virgin material.

Fig. 4 shows a cross section image of a DragonPlate and a G10 sample after 38 seconds of exposure. In both, the line of demarcation between charred material and virgin material is easily visible, though the difference in the G10 sample (Fig. 4b) is much more pronounced.

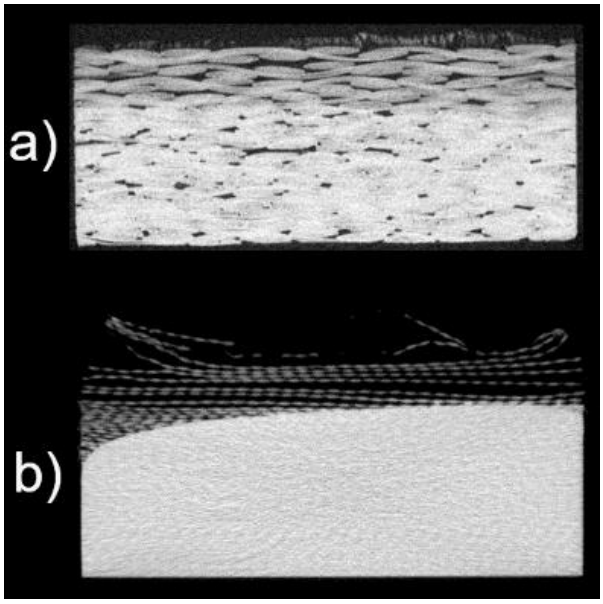


*Figure 4. Cross section of DragonPlate sample (a) and G10 sample (b) x-ray CT scan after 38 seconds of exposure*

By applying a threshold value to the scan volume, a boundary surface can be calculated for the virgin material and for the total extent of the sample, from which the volume of remaining virgin material, $V_v$, and the final volume of the sample, $V_f$, can be calculated. With these values, the initial density $\rho_0$ and the final mass $m_f$, the char density and char volume can be calculated using Eq. 2 and Eq. 3.

$$V_c = V_f - V_v \tag{2}$$

$$\rho_c = \frac{(m_f - \rho_0 V_v)}{V_c} \tag{3}$$

The char depth of the sample was calculated using the average position of the pyrolysis zone within 5 mm of the center of the sample, the approximate location of the stagnation point of the plasma flow. The char depth is reported as the depth relative to the *original* height of the sample to eliminate any ambiguity from variation in the expansion of the char.

## 4 Results

The relationship between the char rate, thermal conductivity, and deflection under load of the various materials was investigated using the measurements made during the plasma tests. The final analysis of the post-insertion material strength test samples has not been performed, so the residual strength of the materials cannot yet be evaluated.

### 4.1 Thermogravimetric Analysis

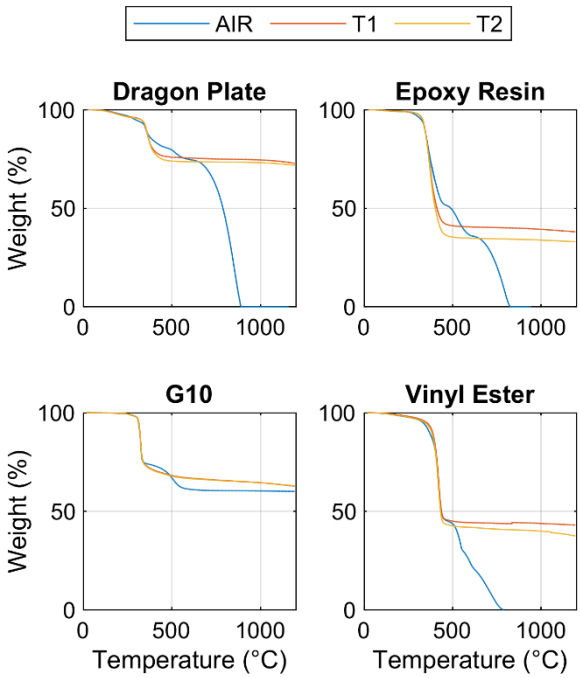


*Figure 5. Thermogravimetric analysis results for four of the materials tested*

Thermogravimetric analysis (TGA) and differential thermal analysis (DTA) were performed on the different materials used in the test campaign. To perform the analyses, samples of material between 25 and 50 mg were exposed to a temperature ramp rate of 10 °C/min from room temperature to 1200 °C using a TA Instruments SDT Q600. Both air and nitrogen were used as purge gases to investigate the difference

between pure thermal degradation and oxidation. The purge gas flow rate was 100 mL/min.

Fig. 5 shows the TGA results for the materials tested. All of the materials show a sharp drop in mass at between 300 °C and 400 °C for both purge gases. However, only the glass fiber composite, G10, fails to completely oxidize when air is used as the purge gas. The other three test materials have completely oxidized by the time they reach 900 °C.

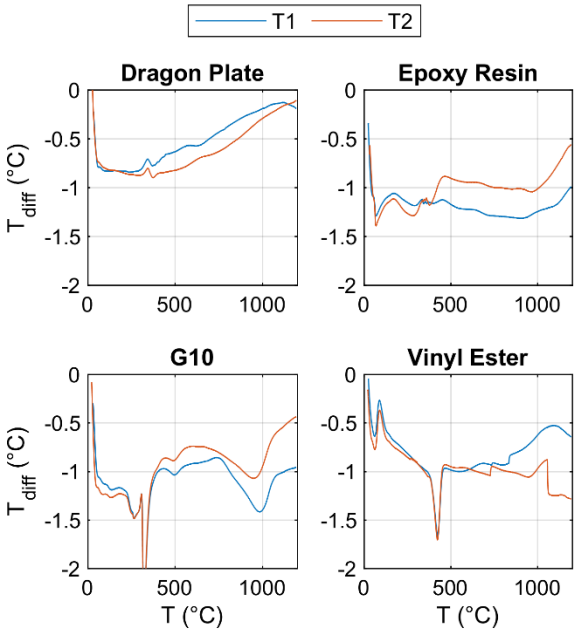


*Figure 6. Differential thermal analysis results for four of the materials tested*

Plots of the temperature difference between the sample and a reference, $T_{diff}$, during the test show the temperatures at which various endothermic and exothermic processes take place. These data are shown for the two inert atmosphere tests of each material in Fig. 6. The spike in temperature difference seen around 400 °C corresponds to the temperature of greatest mass loss rate and the heat excess or deficit from the pyrolysis reaction. For the DragonPlate and the hand-layup epoxy resin samples, this reaction appears to be slightly exothermic while for the G10 (which has a polyester matrix) and hand layup vinyl ester-carbon fiber samples, the reaction is very endothermic. The endothermic spike around 50 °C to 80 °C for both the epoxy resin and vinyl ester resin carbon fiber samples likely corresponds to a drying process as neither of these layups were autoclaved. In addition, the G10 experiences a further endothermic process between 600 °C and 1000 °C that is associated with melting of the glass fibers.

### 4.2 Char Rate

One of the key properties of any charring material in an atmospheric entry case is how fast the pyrolysis front moves through the material, and how much mass is lost during the charring process. The pyrolysis front speed will depend on the applied heat flux and the thickness of the material, so the measured pyrolysis speed is an indicator of the applied heat flux to the material, all things being equal.

#### 4.2.1 Visual Observations

Some qualitative data can be drawn from simple observation of the test samples during and after the tests. Fig. 7 and Fig. 8 show the visual progression of the DragonPlate Economy Plate and G10 samples, respectively, over the duration of the exposure time.

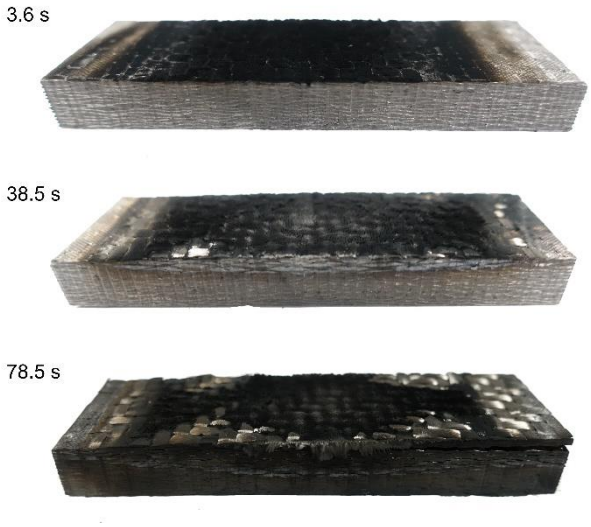


*Figure 7. Photographs of DragonPlate Economy Plate samples after 3.6 s (top), 38.5 s (middle), and 78.5 s (bottom) of exposure*

In the photographs of the DragonPlate samples in Fig. 7, a layer of soot can be seen on the stagnation surface. It is unclear if this layer formed during plasma exposure or after, while the sample was still hot and outgassing. Regardless, it is highly likely that under reentry-type aerodynamic shear conditions, this soot layer would be unable to form.

In the 38.5 s-exposure photograph (middle of Fig. 7) three distinct colors can be discerned on the edge of the plate: a char region, a transition region, and a mostly uncharred region. This is not indicative necessarily of the depth of the char region throughout the sample, as the heat flux is higher at the corners of the sample, but it does show the relative thickness of each region, with the brown transition region being only a millimeter or so thick.

Finally, in the longest exposure sample (bottom of Fig. 7), some delamination of the carbon fiber fabric

layers can be seen. This is an indication that in circumstances where the entirety of a fabric layer is exposed to the flow, aerodynamic shear forces may be able to remove that layer once all of the resin matrix within the fibers has been charred. However, in continuous strand weaves as on COPVs where there is no edge to any given layer, this may not be the case.

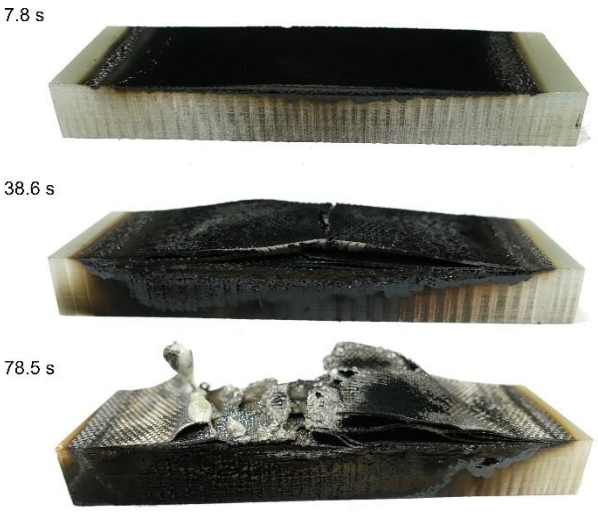


*Figure 8. Photographs of G10 glass fiber reinforced polyester resin samples after 7.8 s (top), 38.6 s (middle), and 78.5 s (bottom) of exposure*

The first detail one might notice in the photographs in Fig. 8 is that several of the fiber layers of the sample have been completely eroded rather than simply charred. Indeed, as the resin pyrolyzed and lost structural integrity, the cloth fibers expanded and peeled away from the bulk of the material where they were more easily melted and spalled off, indicating that glass fiber composites likely are significantly more demisable than carbon fiber-based materials.

### 4.2.2 X-ray Computed Tomography Analysis

For 38 out of the 86 char rate test samples used in the test campaign, X-ray computed tomography (CT) scans were made of the post-exposure samples and analyzed (as described in Section 3.3) to calculate the size and properties of the char layer. Fig. 9 shows the char depth progression over time for DragonPlate, G10, and carbon-fiber/cyanate ester resin composites.

In the current study, the oxidizing plasma resulted in a slower pyrolysis front compared to a non-oxidizing plasma of a similar cold-wall heat flux. This could be due to a reduction in hot-wall heat flux due to removal of oxygen radicals by the reactive gaseous pyrolysis products expelled through the surface of the material.

In contrast to the pyrolysis front speed, the char density, shown in Fig. 10, asymptotically approaches a relatively constant value that is broadly consistent with the char mass to initial mass ratio seen in the TGA data from Fig. 5. Also worth noting is that there is not a significant difference in the char density between the samples exposed to oxidative flow vs. non-oxidative flow. This is not a surprising result, as pyrolysis gas expulsion impedes plasma intrusion into the char layer, and there is no reason to believe that the degree of final charring is that sensitive to applied heat flux.

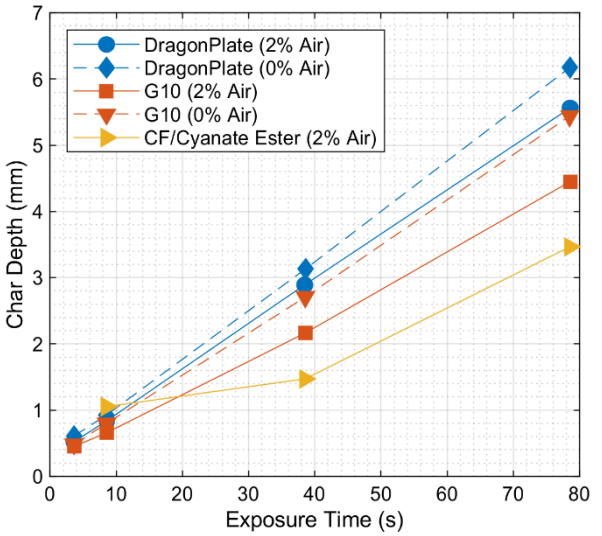


*Figure 9. Measured char depth over time for G10, carbon fiber/cyanate ester resin composite, and DragonPlate samples*

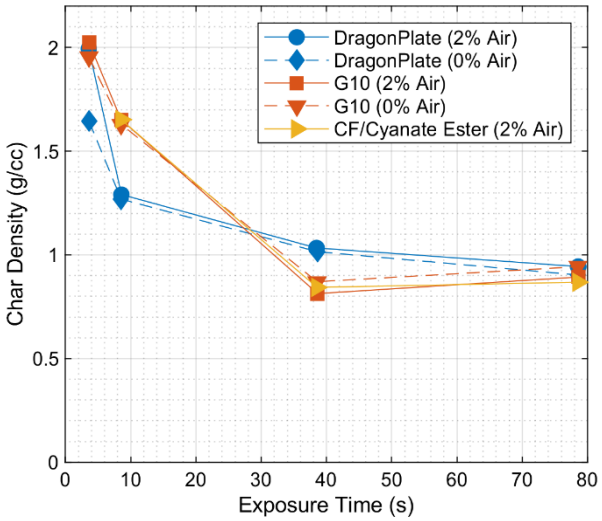


*Figure 10. Measured char density over time for G10, carbon fiber/cyanate ester resin composite, and DragonPlate samples*

Finally, the change in char volume over time, shown in Fig. 11, illustrates another aspect of the charring and ablation of different composite materials. The char volume of the cyanate ester resin composite, for example, is linear over time as would be expected for a linear progression of the char through the depth of the material sample and negligible surface ablation, which

in fact seems to be the case. On the other hand, the rate of increase in the char volume in the DragonPlate sample increases over time. This seems to be due to expansion of the charred material. In contrast, the G10 sample char volume increase rate initially increases due to spreading of the fibers released by charring of the matrix, but then begins to decrease. This is due to surface ablation by melting and subsequent spallation of the glass fibers.

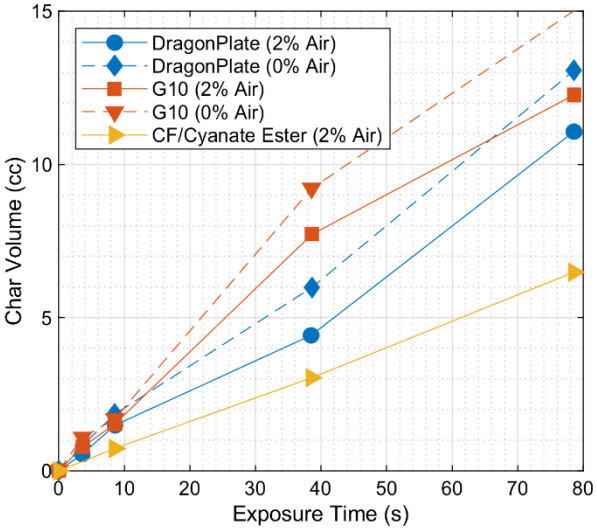


*Figure 11. Measured char volume over time for G10, carbon fiber/cyanate ester resin composite, and DragonPlate samples*

### 4.3 Material Strength

Because the ICP facility used for the current study is a subsonic facility, it is not possible to study the effects of aerodynamic shear on the ablation rate of the material, though some spallation was observed in the glass fiber reinforced samples as droplets of molten glass were blown from the material surface. Instead, to get an idea of how the overall integrity of the material changes with heat absorption, some thin material coupons (< 3 mm thick) were exposed to the plasma under a constant bending load and the surface deflection of the coupon was observed throughout the test using a digital video camera. An example of the type of deflection data obtained is shown in Fig. 12. Digital processing of the video of the sample provides the position of the sample surface within an error of ±0.15 mm at a rate of ~24 frames per second, though in some frames, the brightness of the plasma can interfere with detection of the sample surface.

Unfortunately, the geometry of the sample holder required by the counterweight mechanism and the necessity of keeping the clamp arms out of the plasma places the stagnation point side of the coupon under tensile load. This is the stronger orientation for the sample under the bending load, so failure is observed at a much higher char percentage than would be the case were the force direction to be flipped.

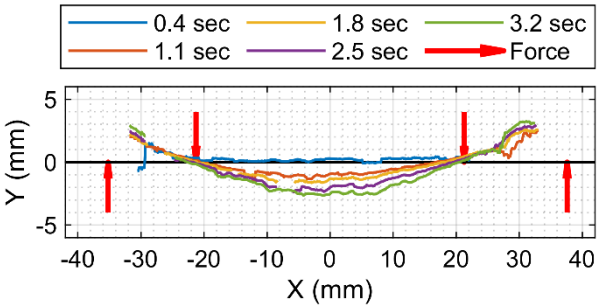


*Figure 12. Example sample deflection data for a wet layup epoxy resin material sample under a 2 N load. The plasma plume is located at x=0 and is flowing in the +y direction.*

Regardless, an estimate of average elasticity, $E_{av}$, of the sample at any point in the test can be calculated from the deflection of the sample by fitting Eq. 4 (where $\delta$ is the vertical displacement, $a$ is the distance between the inner load points, $I$ is the moment of area, and $F$ is the load at each point) to the measured deflection as a function of $x$, assuming the sample is uniform and isotropic. This is not the most accurate, but the calculated elasticity is still a good qualitative indication of the degradation of structural properties.

$$\delta(x) = \frac{Fa}{2E_{av}I}\left(\left(\frac{1}{2}-a\right)^2 - x^2\right) \tag{4}$$

Additionally, the amount of heat absorbed by the sample coupon can be estimated using the control volume analysis depicted in Fig. 13. For simplicity, the heat loss through the edges of the sample is assumed to be negligible due to the relatively small edge surface area. The hot wall heat flux, $q_{hw}$, is calculated from the surface temperature of the sample measured by the pyrometer during the test and the cold wall heat flux measured before the test. The back side-radiative heat loss,$q_{br}$, and stagnation side-radiative heat loss, $q_{sr}$, are calculated using a gray body assumption and the measured back side and stagnation side temperatures, respectively. The heat absorbed by the sample, $Q_{abs}$, is calculated from these heat flux values using Eq. 5.

$$Q_{abs}(t) = \int_0^t \left( A \cdot q_{hw}(t) - A \cdot q_{sr}(t) - \int_A q_{br}(t)\, dA \right) dt \tag{5}$$

Plotting this average elasticity against the total absorbed heat of the sample, as in Fig. 14 to Fig. 16, provides some insights into how the material degrades over time in a re-entry environment.

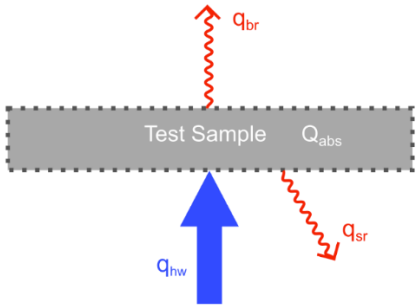


*Figure 13. Control volume analysis of test sample*

On a log-linear plot, the slope of the degradation line is bi-linear. This is most apparent in the DragonPlate samples in Fig. 16 but can be seen in the wet layup epoxy samples in Fig. 14, and to a lesser extent in the vinyl ester samples in Fig. 15.

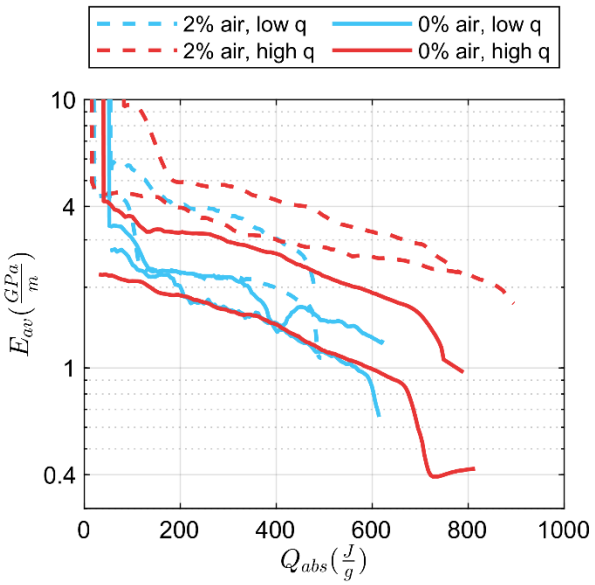


*Figure 14. Calculated average elasticity of the wet layup carbon fiber/epoxy resin material as a function of absorbed heat for each test condition*

The spread in average elasticity values between tests is also seen to be much larger for the wet layup samples than for the DragonPlate samples. This is likely because the DragonPlate samples are a commercial off-the-shelf product, and the wet layup samples were laid up by hand in a NASA JSC machine shop and may have been subject to more variability in matrix infusion and between specimens.

Some individual tests show a dip in elasticity before recovering, especially at lower values of absorbed heat. This is an artifact of the image processing algorithm being unable to find the true surface of the sample due to interference from the incandescence of the charring and ablation products in the plasma.

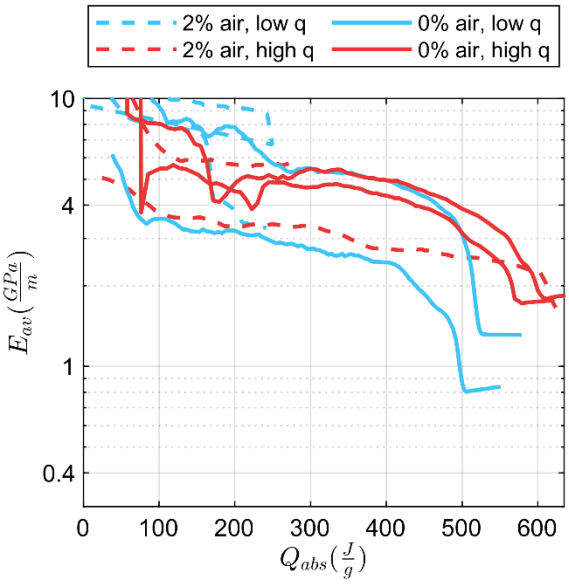


*Figure 15. Calculated average elasticity of the wet layup carbon fiber/vinyl ester material as a function of absorbed heat for each test condition*

Also indicated in Fig. 14 to Fig. 16 are heat absorption limits for each test and the breakpoint $Q_{abs}$ at which the rate of structural degradation increases. The heat absorption limit, where the sample experienced complete structural failure, is indicated by the sharp downturn at the end of each plot before the data is cut off by the loss of the sample. Comparisons of these values for the various materials and test conditions are given in Fig. 17 and Fig. 18, respectively.

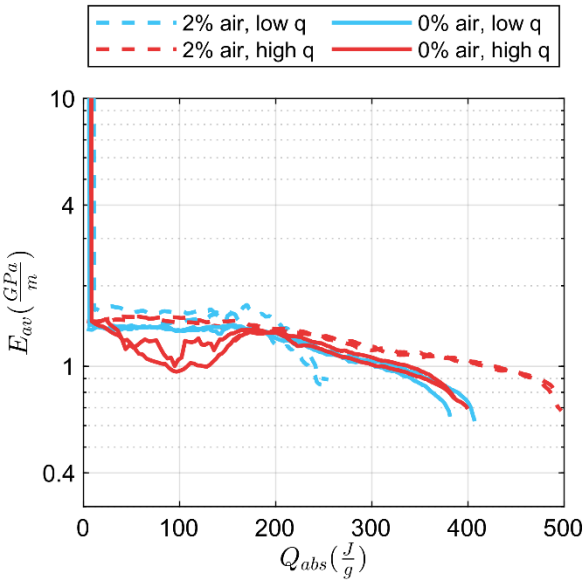


*Figure 16. Calculated average elasticity of the DragonPlate carbon fiber/epoxy material as a function of absorbed heat for each test condition*

Variability in the degradation breakpoint, shown in Fig. 17, is extremely low for the DragonPlate Economy

Plate samples, but varies by as much as 150 °C for the vinyl ester -and wet layup-epoxy matrix samples. This could be significant, but is likely due to more variability in the hand-made samples.

More surprising is the difference in failure point between the DragonPlate and the wet layup epoxy samples. In some of the tests, the wet layup samples were able to absorb almost twice as much specific heat as the DragonPlate samples before ultimate failure.

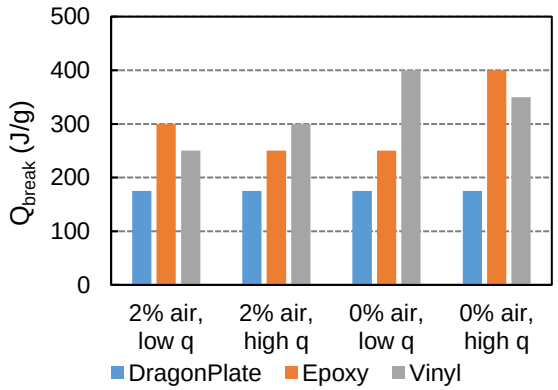


*Figure 17. Degradation breakpoint heat absorption for each material and test condition*

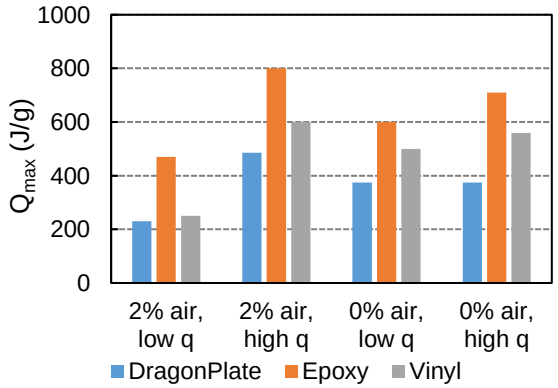


*Figure 18. Heat absorption structural failure point for each material and test condition*

#### 4.3.1 Cyanate Ester and Phenolic

Even under the highest load tested, the DragonPlate High Temp samples did not deflect at all during an 80 s test under any conditions. Given the results from the char analysis, this is more than enough time for the entire sample to have charred through, indicating that a significant amount of the matrix material remains as char material with enough integrity to hold the fibers together.

The cyanate ester materials, on the other hand, eventually exhibited structural degradation under the test conditions, though the failure did not manifest as a reduced elasticity. Rather, the cyanate ester samples remained straight along most of the length and creased at one or both of the inner load points at some time after 50 seconds of exposure.

## 5 Modeling

Based on these test results, the authors have developed a charring and ablation model for G10, carbon fiber-epoxy, and carbon fiber-polyester composites. The model is based on that proposed by Hidalgo, *et al.* [6] and uses TGA data for the specific materials used in the char testing to calculate a remaining mass as a function of temperature. The temperature of the sample is calculated using a finite difference thermal transport model assuming an inert material, and then the updated temperature is used to calculate an updated char fraction.

### 5.1 Assumptions

Several simplifying assumptions were made to implement the model more easily.

- Expansion in char material is negligible
- Interior charring is a completely anoxic process
- The mass loss in a mesh cell is equal to the mass loss in a TGA sample of the material at the mesh cell temperature
- The thermal conductivity and thermal capacity of the char material is equal to that of bare woven fibers in air.

### 5.2 Mass Loss Model

The TGA data shown in Section 4.1 were compiled in MATLAB and functions were fit piecewise to the curves for fast evaluation. The assumption of anoxic charring allows for the exclusion of the air-purged TGA data sets; only the nitrogen-purged TGA will be used to calculate the char mass loss. In addition, complete data sets only exist for the DragonPlate and G10 materials, so these are the only two materials that will be discussed.

The mass loss of the DragonPlate material with increasing temperature can be seen in Fig. 19 (run T2 is chosen as the exemplar), along with a 4-region piecewise fit. The fit functions for each region are defined as in Eq. 6 through Eq. 9.

$$m_{frac}(T) = 1\,, (T < 100°C) \tag{6}$$

$$m_{frac}(T) = 1.0235 - 2.346 \times 10^{-5} \cdot T, \quad (100°C \leq T < 343°C) \tag{7}$$

$$m_{frac}(T) = 4.9943 - 0.0195\,T + 2.2413 \times 10^{-5}\,T^2, \quad (343°C \leq T < 435°C) \tag{8}$$

$$m_{frac}(T) = 0.7724 - 4.4837 * 10^{-5}\, T, \quad (435°C \leq T < 1200°C) \tag{9}$$

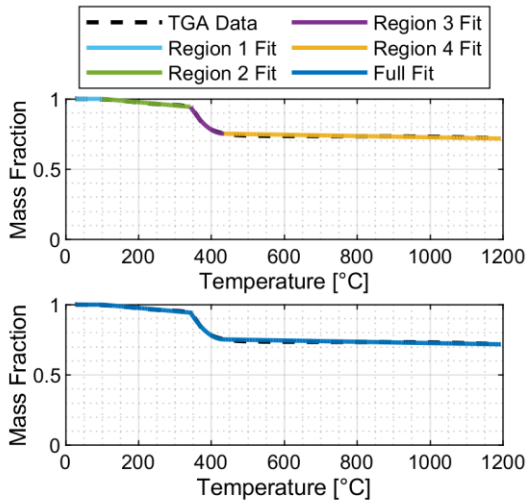


*Figure 19. Remaining mass fraction of DragonPlate composite with increasing temperature (T2 run), including fit functions*

Similarly, the mass loss of the G10 material with increasing temperature can be seen in Fig. 20 (run T1 chosen as the exemplar); the fit functions for each region are defined as in Eq. 10 through Eq. 14.

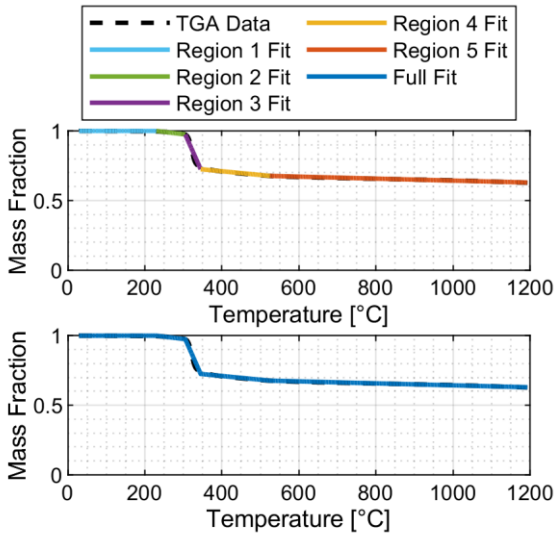


*Figure 20. Remaining mass fraction of G10 composite with increasing temperature (T1 run), including fit functions.*

$$m_{frac}(T) = 1, (T < 230°C) \tag{10}$$

$$m_{frac}(T) = 1.0767 - 3.333 * 10^{-4} * T, (230°C \leq T < 305°C) \tag{11}$$

$$m_{frac}(T) = 2.8813 - 0.00625 * T, (305°C \leq T < 345°C) \tag{12}$$

$$m_{frac}(T) = 0.817 - 2.667 * 10^{-4} * T, (345°C \leq T < 525°C) \tag{13}$$

$$m_{frac}(T) = 0.7143 - 7.111 * 10^{-5} * T, (525°C \leq T < 1200°C) \tag{14}$$

### 5.3 Finite Difference Model

Now that a model for mass loss with temperature has been developed, it must be combined with a thermal transport model to calculate the char depth as a function of time. A new time-accurate finite difference code was developed to simulate the char depth test using material properties from the ORSAT material database and the recently-developed TGA mass fraction models. The algorithm implemented to solve this problem is outlined as follows:

- Compute the heat transfer into the front face (including the plasma jet and radiation)
- Compute the thermal conduction between all nodes
- Compute the thermal radiation from the back face
- Compute new nodal temperatures from net heat transfer per node
- Update the temperature-varying material properties
- Iterate on the nodal temperatures and heat fluxes during a time step until they converge
- Update the mass fraction for each node, then continue to the next time step and perform the process again

Some potential sources of uncertainty in this model include: the areas of the front face which do not receive heating from the plasma torch, but do have heat conducted and radiated away; variation in thermal properties away from the ORSAT database materials; and pyrolysis shielding from the plasma torch or removing heat through outgassing.

### 5.4 Model Results

The finite difference model simulations were run for the G10 and DragonPlate materials, emulating the char depth tests. Four fiducial points were used for each material to assess the progression of the char during a test.

The G10 model, with constant thermal properties, was quick to run, completing in approximately 12 hours (vs. 78.5 seconds of simulated time). The char depth for G10 is determined as the location where the mass fraction decreases to 70% of the pristine material, based on the final mass of the TGA test in Fig. 20. The temperature distribution and char depth progression through the simulated sample can be seen in Fig. 21. The simulated and actual char depth results are compared in Tab. 3.

*Table 3. Comparison of simulated char depth with sample test results for G10*

| Time (sec) | $D_{char}$ (mm) | Simulated $D_{char}$ (mm) | δ (mm) | δ (%) |
|---|---|---|---|---|
| 3.6 | 0.48 | 0.41 | -0.07 | -15% |
| 8.5 | 0.80 | 1.0 | 0.2 | 25% |
| 38.5 | 2.7 | 3.1 | 0.4 | 15% |
| 78.5 | 5.4 | 5.1 | -0.3 | -6% |

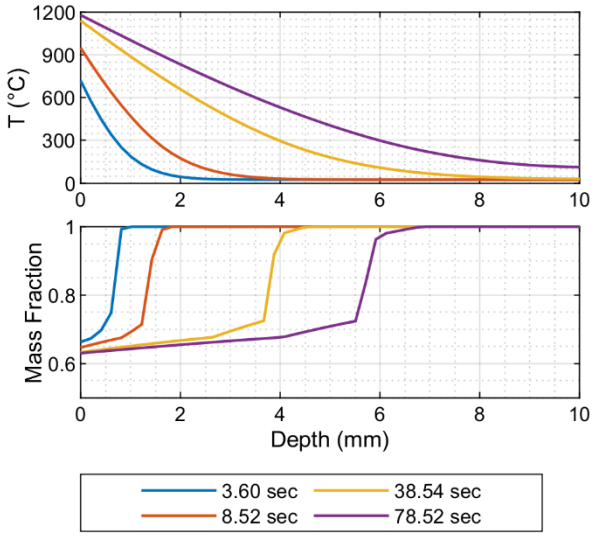


*Figure 21. Temperature and mass fraction profiles of the simulated GFRP material at the fiducial time points in the G10 test samples*

The DragonPlate model, with its temperature-varying thermal properties, required approximately 40 hours to run (with 78.6 seconds of simulated time), significantly longer than the G10 model. The char depth for DragonPlate is determined as the location where the mass fraction decreases to 75% of the pristine material, based on the final mass of the TGA test in Fig. 19. This simulation delivered comparable results, with the plots of temperature distribution and char depth progression through the simulated sample seen in Fig. 22. The simulated and actual char depth results are compared in Tab. 4.

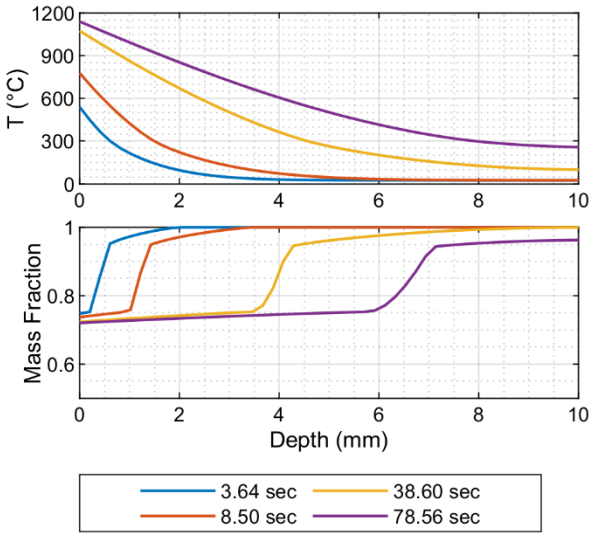


*Figure 22. Temperature and mass fraction profiles of the simulated CFRP material at the fiducial time points in the DragonPlate test samples*

*Table 4. Comparison of simulated CFRP char depth with measured char depth in DragonPlate sample*

| Time (sec) | $D_{char}$ (mm) | Simulated $D_{char}$ (mm) | δ (mm) | δ (%) |
|---|---|---|---|---|
| 3.6 | 0.61 | 0.2 | -0.41 | -70% |
| 8.5 | 0.92 | 1.0 | 0.08 | 7% |
| 38.6 | 3.1 | 3.4 | 0.3 | 10% |
| 78.6 | 6.2 | 5.9 | -0.3 | -5% |

Finally, a fine-grained comparison of the simulated char progression and the test data can be seen for G10 and DragonPlate in Fig. 23 and Fig. 24, respectively. Both simulations agree well with the test data, though the simulated pyrolysis front pulls ahead of the measured data around the 40-second point before slowing down and matching the test data again by the 80-second mark. The likeliest source of this discrepancy is the 3D nature of the charring process in the plasma torch tests.

As another check of the model's accuracy, the measured and simulated front- and back-surface temperature profiles can be compared. These profiles are shown in Fig. 25 and Fig. 26 for G10 and DragonPlate, respectively. It is relatively clear from both of these figures that the thermal conductivity used to simulate both the G10 and the DragonPlate is a little too high, as the simulated back side temperature overshoots the measured temperature by 20–50 K. A lower conductivity would also cause the front side temperature to better match the measurements, as a lower conduction rate into the material would cause the simulated front side temperature to rise much more rapidly and plateau at a slightly higher temperature.

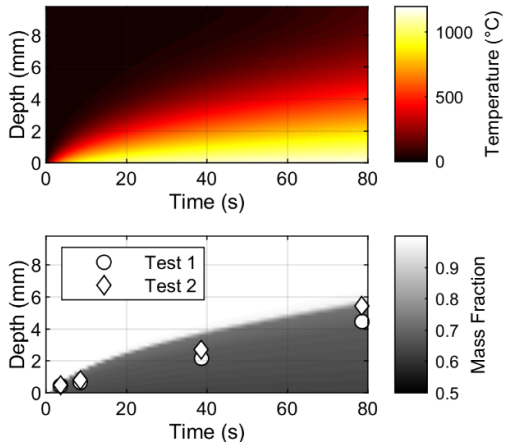


*Figure 23. G10 simulated temperature and mass fraction distribution vs. time, compared to the measured char depth in the test samples*

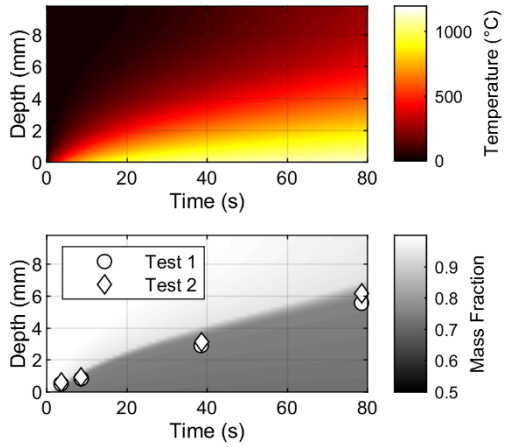


*Figure 24. DragonPlate simulated temperature and mass fraction distribution vs. time, compared to the measured char depth in the test samples*

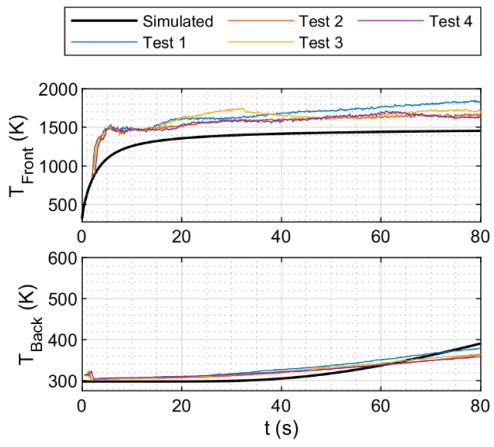


*Figure 25. Comparison of simulated temperature in GFRP to the measured front (top axes) and back (bottom axes) surface temperatures from four different tests using G10*

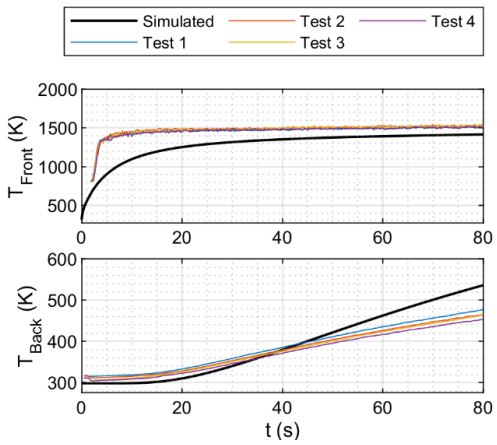


*Figure 26. Comparison of simulated temperature in CFRP to the measured front (top axes) and back (bottom axes) surface temperatures from four different tests using DragonPlate*

For the GFRP material in Fig. 25, especially, some of the mismatch in the front side temperature is due to uncertainty in the appropriate surface emissivity to apply to the pyrometer measurement. A surface emissivity of 0.86 is assumed, but as the surface chars, this value will very likely increase to 0.9 or 0.92, causing a significant error in the reported front surface temperature value.

## 6 Conclusion

The NASA ODPO conducted an extensive test series to improve understanding of the behavior of glass- and carbon fiber-reinforced polymers in a realistic reentry thermal environment.

Novel techniques such as X-ray CT scans and in-situ 4-point bending load application to the test samples were used to measure the charring rate and strength degradation of several different fiber-reinforced polymers. Future work includes cross-sectioning selected samples to compare to X-ray CT scans and measuring the post-exposure strength of selected test coupons in a laboratory 4-point bend configuration to compare to the in-situ results presented here.

A new thermal charring model ready for implementation into ORSAT was developed using thermogravimetric analysis data and validated against char depth rate tests in the University of Texas at Austin plasma torch facility. The thermal charring model was found to agree well with the available test data in terms of both char depth and front- and back-side temperature profiles for both materials examined. Future improvements to the model include using more accurate char material thermal conductivity and thermal capacity values from the literature and including the effect of the heat of pyrolysis on the effective thermal capacity.

The new charring model, together with further enhancements of the surface ablation and spalling models that can be made using this test data, will improve the ability of the ODPO to accurately predict the ground casualty risk for atmospheric disposal of modern spacecraft with a large number of composite structures.

## 7 References


1. Greene, B.R., & Sanchez, C.M. (2019). Demisability of GFRP and CFRP Components of Reentering Orbital Debris: Phase I Test Results. In *10th International Association for the Advancement of Space Safety Conference*, El Segundo, CA.

2. Lips, T., Fritsche, B., Kanzler, R., Schleutker, T., Gülhan, A., Bonvoisin, B., Soares, T., & Sinnema, G. (2016). About the Demisability of Propellan Tanks During Atmospheric Re-Entry from LEO. In *8th International Association for the Advancement of Space Safety Conference*, Melbourne, FL.

3. Griffis, C.A., Masumura, R.A., & Chang, C.I..(1981). Thermal Response of Graphite Epoxy Composite Subjected to Rapid Heating. US Naval Research Laboratory, Washington, D. C..

4. Blasi, C.D. (2000). The State of the Art of Transport Models for Charring Solid Degradation. *Polymer International.* **49**(10), pp1133-1146.

5. Gibson, A.G., Feih, S., & Mouritz, A. (2011). Developments in Characterising the Structural Behaviour of Composites in Fire. In *Composite Materials: A Vision for the Future*, (Eds. L. Nicolais, E. Milella & M. Meo) London, U.K., Springer, pp187-217.

6. Hidalgo, J.P., Pironi, P., Hadden, R.M., & Welch, S. (2015). A Framework for Evaluating the Thermal Behavior of Carbon Fibre Composite Materials. In *Proceedings of the 2nd IAFSS European Symposium of Fire Safety Science*, Nicosia, Cyprus.

7. McKinnon, M.B., Ding, Y., Stoliarov, S.I., Crowley, S., & Lyon, R.E. (2017). Pyrolysis Model for a Carbon Fiber/Epoxy Structural Aerospace Composite. *Journal of Fire Sciences.* **35**(1), pp36-61.

8. Quang Dao, D., Luche, J., Richard, F., Rogaume, T., Bourhy-Weber, C., & Ruban, S. (2013). Determination of Characteristic Parameters for the Thermal Decomposition of Epoxy Resin/Carbon Fiber Composites in Cone Calorimeter. *International Journal of Hydrogen Energy.* **38**(19), pp8167-8178.

9. Kucner, L. (1992). *Experimental Investigation of Fire Damage to Composite Materials.*, Boston, MA: Massachusettes Institute of Technology, Department of Aeronautics and Astronautics,

10. Biasi, V., Leplat, G., Feyel, F., & Beauchêne, P. (2014). Heat and Mass Transfers Within Decomposing Carbon Fibers/Epoxy Resin Composite Materials. In *11th AIAA/ASME Joint Thermophysics and Heat Transfer Conference*, Atlanta, GA.

11. Di Modica, P. (2016). Modelling Fire Behaviour of Composite Materials. School of Mechanical and Systems Engineering, Newcastle University.

12. Hill, D.J., & Torero, J.L. (2004). Experimental Characterization of the Effect of Charring on the Residual Load Carrying Capacity of a Structural Fibre Reinforced Composite. In *10th Interflam*, Edinburgh, UK.

13. Kandare, E., Kandola, B.K., Myler, P., & Edwards, G. (2010). Thermo-Mechanical Responses of Fibre-Reinforced Epoxy Composites Exposed to High Temperature Environments. Part I: Experimental Data Acquisition. *Journal of Composite Materials.* **44**(26), pp3093-3114.

14. Bai, Y., Post, N.L., Lesko, J.J., & Keller, T. (2008). Experimental investigations on temperature-dependent thermo-physical and mechanical properties of pultruded GFRP composites. *Thermochimica Acta.* **469**(1-2), pp28-35.

15. Burns, L.A., Feih, S., & Mouritz, A. (2009). Fire-Under-Load Testing of Carbon Epoxy Composites. In *47th Aerospace Sciences Meeting*, Orlando, FL.

16. Greene, B.R., Clemens, N.T., Varghese, P.L., Bouslog, S., & Del Papa, S.V. (2017). Characterization of a 50 kW Inductively Coupled Plasma Torch for Testing of Ablative Thermal Protection Materials. In *AIAA SciTech Forum - 55th AIAA Aerospace Sciences Meeting*, Grapevine, TX.